Ab initio calculation of the bias-dependent transport properties of Mn_{12} molecules

C. D. Pemmaraju, I. Rungger, and S. Sanvito
School of Physics and CRANN, Trinity College, Dublin 2, Ireland
(Received 19 June 2009; published 17 September 2009)

The bias-dependent transport properties of a device constructed by sandwiching a Mn_{12} single molecule magnet between gold electrodes are investigated within an *ab initio* framework combining the nonequilibrium Green's function approach with density-functional theory. The self-consistently calculated current-voltage, *I-V*, curves exhibit characteristic negative differential resistances. These originate from the interplay between electron localization and the rehybridization of the Mn_{12} molecular levels in an external electric field. Interestingly, such features in the transport are sensitive to the internal spin configuration of the molecule. This may therefore enable one to infer the internal spin state of the molecule from a detailed knowledge of the *I-V*.

DOI: 10.1103/PhysRevB.80.104422 PACS number(s): 75.50.Xx, 85.65.+h, 73.23.−b, 85.75.−d

I. INTRODUCTION

The possibility of addressing and manipulating single spins represents the ultimate limit for the magnetic data storage industry. It may also lead to a technological platform for the integration of logic- and data-storage functionalities on the same device. Towards this end, single molecule magnets (SMMs) such as Mn_{12} represent a promising class of materials and have in recent times been the focus of intense research.[1] The properties of these SMMs in their single crystalline forms are well understood and current experimental and theoretical efforts are geared towards investigating the properties of SMMs deposited on metal surfaces or incorporated into nanodevices.

Two experiments have recently measured the *I-V* curve of three-terminal devices using Mn_{12} as the resistive element,[2,3] in both cases revealing features associated to the magnetic state of the molecule. Negative differential resistances (NDRs) have been tentatively ascribed to selection-rule forbidden transitions between different charging and spin states,[4,5] although a direct quantitative analysis of the results is complicated by the large variation in *I-V*s from device to device and by the low device production yield. This stems from the general fragility of Mn_{12} in single molecule form on surfaces against fragmentation[6] and redox.[7] The spectroscopical detection of Mn^{2+} in a Mn_{12} monolayer[6,7] is proof of such fragility. Furthermore, when the molecule remains intact without changing its oxidation state, still the magnetic response is rather sensitive to the surface environment and different from that of a single crystal. Most notably the anisotropy disappears,[8] making the interpretation of the transport features in terms of selection-rule-forbidden transitions more complicated.

Nevertheless, these pioneering transport measurements provide an indirect evidence for the different spin states of the molecule. In addition to such three-terminal measurements studying the low-energy excitation spectra of these molecules, scanning tunneling microscopy (STM) measurements that probe the band gap and the single-particle levels of the molecule have also been reported.[9]

On the theoretical front, most of the investigations on the electronic-transport properties of SMMs reported to date have been based on model Hamiltonian approaches employing parameters extracted from ideal single-crystal properties.[10–13] Within this framework, many interesting dynamical effects involving quantum tunneling,[10] current-induced magnetic switching,[11] cotunneling,[12] and Kondo effect[13] have been demonstrated. However, model Hamiltonian calculations do not fully take into account the effects of molecule-metal interfaces and of the device geometry which can have a significant effect on the transport properties. Therefore *ab initio* approaches appear as necessary to additionally complement the results obtained from model approaches. Still, owing to the large system size typically associated with SMMs and also the complexity of the electron Hamiltonian needed to describe them, first-principles modeling of these systems has not been very tractable so far. While the advent of efficient and scalable numerical algorithms[14,15] has tackled the system size problem to some extent, the modeling of strong correlations and time-dependent effects in transport through SMMs within a first-principles framework remains a challenge. As far as we know the zero-bias work of Barraza-Lopez *et al.*[16] remains the only attempt at calculating the transport properties of SMMs from first principles.

Currently, the most commonly used *ab initio* method for out of equilibrium electron-transport simulations is based on a mean-field approach that combines the nonequilibrium Green's function (NEGF) formalism with density-functional theory (DFT).[14] In general a mean-field treatment is not ideally suited for describing the properties of weakly coupled or strongly correlated transport systems. However one can still calculate useful quantities, such as the bias-dependent electron-hopping parameters, and the transport properties for level occupancies close to integer values.[17] Note that some improvements within the mean-field description of transport can be achieved by incorporating strong-correlation effects at the DFT level. This is commonly done through on-site corrections such as LDA+*U* or self-interaction correction.[18,19] In this work, we present the self-consistent finite-bias *I-V* characteristic up to an applied bias of 0.4 eV for a Mn_{12} molecule sandwiched between nonmagnetic Au electrodes. The effect of Hubbard-*U* corrections on the zero-bias transport properties are also investigated. Furthermore, we compare the electrical response of two different internal spin configurations of the molecule. First we look at the ground state (GS), where the spins of the eight peripheral Mn^{3+} ions align antiparallel to those of the inner Mn^{4+} to give an over-

all $S=10$ spin state.[1] The second is a spin-flip (SF) configuration in which the spin directions of one Mn^{3+} and one Mn^{4+} are reversed with respect to those in the GS. The total spin projection for such a state is $S=9$.[20]

The most notable difference between the I-V curves obtained for the different spin states is the much higher low-bias current of the GS configuration and the presence of NDRs, which are specific to the spin state. These are a consequence of orbital rehybridization under bias, which causes a highly nonlinear bias-dependent coupling of the molecular levels to the electrodes. We predict that this is a general feature of molecular junctions characterized by closely spaced orbital multiplets, such as those appearing in magnetic molecules. Importantly, since both the orbital symmetry and their localization depend on the molecule's spin state, we expect different I-V fingerprints for different magnetic configurations. This means that the overall molecular magnetic configuration is readable entirely from a single nonspin-polarized current readout.

II. COMPUTATIONAL METHOD

Density-functional total-energy calculations and geometry optimizations are performed using the SIESTA (Ref. 21) code which employs a numerical localized orbital basis set and norm-conserving pseudopotentials. The generalized gradient approximation (GGA) (Ref. 22) is used for the exchange-correlation functional. Some calculations employing the LDA+U (Refs. 23 and 24) method are also presented for comparison. We use standard scalar relativistic pseudopotentials with the following reference configurations: H $1s^1$, C $2s^22p^2$, S $3s^23p^4$, O $2s^22p^4$, Mn $4s^23d^5$, and Au $6s^1$. The atomic basis set is constructed as follows: C:DZ-s, DZ-p; H:DZP-s; O:DZ-s, DZP-p, SZ-d; S:DZ-s, DZP-p, SZ-d; Mn:DZP-s, SZP-p, DZ-d; and Au:DZ-s (the notation is SZ=single zeta, DZ=double zeta, and P=polarized).[21] The real-space grid has an equivalent cutoff energy of 400 Ry.

Transport calculations are performed with the SMEAGOL code,[14,15] which combines the NEGF,[25,26] with DFT as implemented in SIESTA.[21] The charge density is obtained by splitting the integral of the Green's function (GF) into a contribution calculated over the complex energy plane and one along the real axis.[14] The complex integral is performed over a uniform mesh of 512 imaginary energies while for the real part we have implemented a mesh refinement algorithm, necessary to integrate the extremely sharp features of the density of states (DOS). Such an algorithm consists in evaluating the integral over an initial coarse energy mesh after the GF has been artificially broadened. Then peaks in the GF are detected and a denser energy mesh is generated around them. The next approximation is then calculated over this new grid after the artificial broadening has been decreased. Such a procedure is repeated until no artificial broadening is left. Typically the final mesh includes 1000 energy points with the denser energy spacing being around 10^{-5} eV. Furthermore, in order to boost the convergence especially in view of the large system size, a number of technical solutions including a recently developed singularity removal procedure to evaluate accurately the leads self-energies,[27] have been implemented.

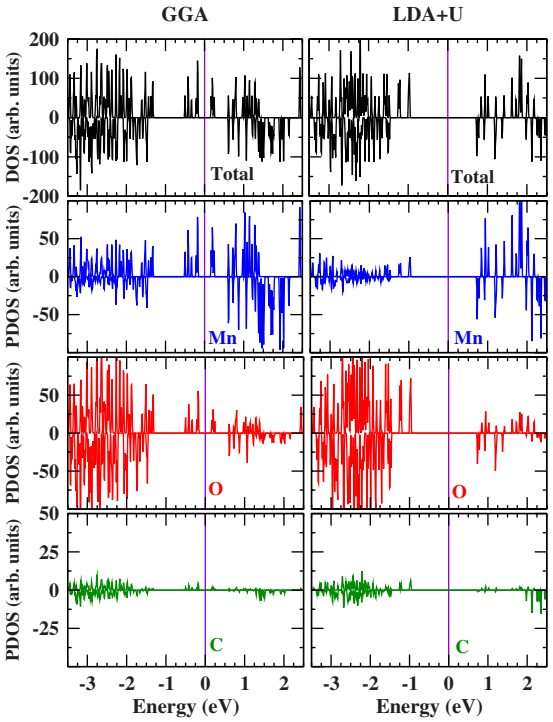

FIG. 1. (Color online) Spin- and orbital-resolved density of states around the Fermi level (vertical line at 0) for $[Mn_{12}O_{12}(CH_3COO)_{16}(H_2O)_4]$ in the $S=10$ ground state. Positive values correspond to majority spins, negative values to minority spins. Note the strong Mn-O hybridization both in the HOMO and LUMO manifold of states with relatively little C $2p$ intermixing. The HOMO-LUMO gap is underestimated in GGA but it is corrected close to the experimental value with LDA+U.

III. DFT ELECTRONIC STRUCTURE

The ground-state electronic structure of Mn_{12}, within the context of DFT, has been studied previously by many groups and is generally well understood.[28–31] Here we present a brief overview of the electronic structure of the Mn_{12} acetate cluster $[Mn_{12}O_{12}(CH_3COO)_{16}(H_2O)_4]$ mainly to setup the framework for the transport results to follow. The spin-resolved DOS around the Fermi level, calculated using both GGA and LDA+U ($U=6$ eV, $J=0.9$ eV), is presented in Fig. 1. As a general feature common to both functionals, the highest-occupied molecular orbital (HOMO) and lowest-unoccupied molecular orbital (LUMO) manifold of states are comprised predominantly of hybridized Mn $3d$ and O $2p$ states with a relatively small mixing with C $2p$ orbitals. Thus the charge density corresponding to these states is expected to be primarily localized on the Mn-O core of the molecule. Furthermore, both in GGA and LDA+U the HOMO manifold is built from occupied e_g orbitals derived from the eight Mn^{3+} ions (see Fig. 2). Note that there are no occupied minority-spin levels within $\sim$0.5 eV of the HOMO states.

As it is typically the case in transition-metal oxide systems,[32] the HOMO-LUMO gap in GGA is underestimated at 0.35 eV relative to the experimental gap of $\sim$1.4 eV.[33] This is rectified by incorporating strong correlations at the level of LDA+U which opens up the gap to 1.6 eV. In addition to the gap, the other main difference in the DOS be-

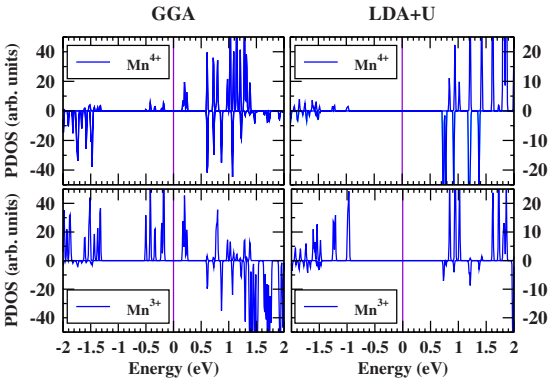

FIG. 2. (Color online) Density of states from Mn ions around the Fermi level (vertical line at 0) for $[Mn_{12}O_{12}(CH_3COO)_{16}(H_2O)_4]$ in the $S=10$ ground state obtained from GGA (left) and LDA+U (right). The contributions from Mn^{4+} (top) and Mn^{3+} (bottom) ions are shown separately. Note that the HOMO manifold is build mainly from Mn^{3+}-derived states.

tween GGA and LDA+U is the nature of the LUMO state. While in GGA the LUMO is also a majority-spin Mn^{3+}-derived state, in LDA+U it is a minority-spin Mn^{4+}-derived state. These results are in good agreement with the LDA+U results of Boukhvalov *et al.*[31]

We now compare the GGA electronic structure of the GS configuration with the SF configuration. As mentioned previously, the SF configuration is generated by flipping the local spin on two Mn ions (one Mn^{3+} and one Mn^{4+}) to give a total spin projection of $S=9$. The SF configuration is found to be ~156 meV higher in energy than the GS configuration. Note that this spin-flip state, being a single-determinant DFT solution, does not directly correspond to any of the low-energy spin-multiplet excitations of the $S=10$ ground state of Mn_{12} which occur at much lower energies.[34] Nevertheless, it is helpful in analyzing the effect of the local spin configuration of the Mn-O core on the transport properties of the molecule.

In Fig. 3 we show the spin-resolved DOS and the associated local DOS for a few of the molecular orbitals around the Fermi energy (E_F) for both the GS and SF configurations. In the GS the DOS is entirely spin polarized around E_F with a set of three almost degenerate levels forming the HOMO, followed by a singly degenerate HOMO-1. Such an orbital composition of the HOMO is maintained also when the Hubbard-U corrections are applied. The degeneracy is then lifted in the SF configuration, where the HOMO is now formed by four closely spaced Mn^{3+} levels, one of which has the opposite spin. Overall the total DOS (not considering the spin polarization) is rather similar in the two cases, suggesting that an electrical measurement, which is not sensitive to

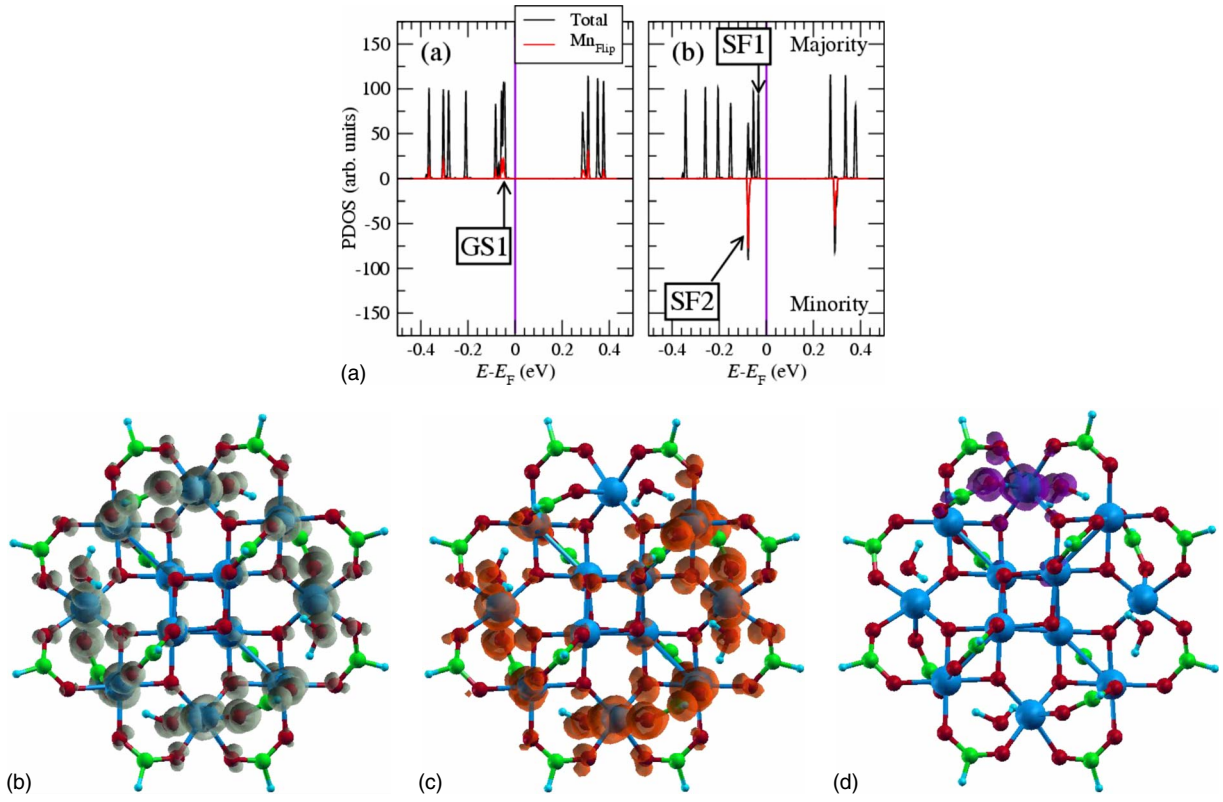

FIG. 3. (Color online) Density of states around the Fermi level (vertical line at 0) for $[Mn_{12}O_{12}(CH_3COO)_{16}(H_2O)_4]$ in the (a) ground state and the (b) spin-flip state. Mn_{Flip} indicates the Mn^{3+} ion whose spin direction was flipped when constructing the SF state. The lower panels display charge-density isosurfaces (local density of states), respectively, for the GS HOMO (GS1), and for both the HOMO (SF1) and the HOMO-4 (SF2) of the SF configuration. Note that SF2 has opposite spin direction with respect to the remaining HOMOs around E_F. Color code for spheres representing atoms: blue=Mn (large, dark gray), red=O (small, dark gray), green=C (small, light gray), and light blue=H (very small, light gray).

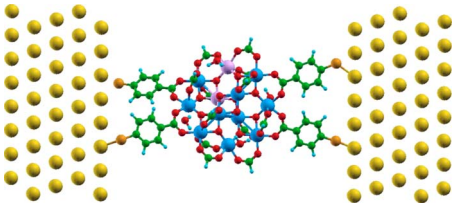

FIG. 4. (Color online) Transport simulation cell used in this work. Color code: blue=Mn, red=O, green=C, light blue=H, yellow=Au, dark yellow=S, purple=Mn (flipped).

the spin direction, will hardly be able to distinguish between them. However there is an important difference between the two configurations. This is the degree of localization of the various HOMO levels. In the GS the local DOS shows amplitude uniformly distributed around all the eight Mn^{3+} ions while in the SF state the minority HOMO is extremely localized around the flipped Mn^{3+} ion. This has a profound influence over the electrical response of the molecule.

IV. TRANSPORT SETUP

The transport simulation cell is constructed from a $[Mn_{12}O_{12}(CH_3COO)_{16}(H_2O)_4]$ molecule comprising 16 thiol-terminated C_6H_4 ligands. We cut 12 of those 16 organic ligands and passivate the remaining bonds in order to reduce the lateral size of the cell. The final molecule is relaxed in vacuum by a standard conjugate gradient method and then positioned at a minimal energy location on the Au (111) surface. The search for the minimum is conducted as follows. First we place the S atom of one of the remaining four ligands at the hollow site of the Au (111) surface. This is one of the preferential bonding sides for thiol on Au (111).[17] Then we rotate the molecule about this position in the search of the total-energy minimum.

The device simulation cell also includes five Au atomic planes on each side of the molecule. The lateral dimensions of these are those of a 6×4 supercell constructed from the primitive cell along the fcc (111) direction. The unit cell for the electrodes is also a 6×4 supercell. A lattice constant of $a=4.1812$ Å is used for Au. The resulting scattering region (where the self-consistent calculation takes place) is presented in Fig. 4. Note that in the figure two of the 12 Mn atoms are colored in purple (light gray) while the other ones are blue (dark gray). These are the ions whose spins are flipped in forming the SF configuration of the molecule. The final simulation cell contains 620 atoms, of which 480 are Au atoms of the electrodes, with the basis set expanding over 2672 local orbitals for each spin direction.

Note that the electronic structure of the $Mn_{12}O_{12}$ core of the molecule is insensitive to the presence of the attached organic functional groups and essentially retains all the properties of the Mn_{12} cluster described previously. The organic functional groups do not introduce any new states in the region around E_F. Furthermore, we find that attaching the molecule to Au electrodes also has no significant effect on the electronic structure (Fig. 5). The organic functional groups act as spacers to reduce the interaction between the $Mn_{12}O_{12}$ core and the Au(111) surface.

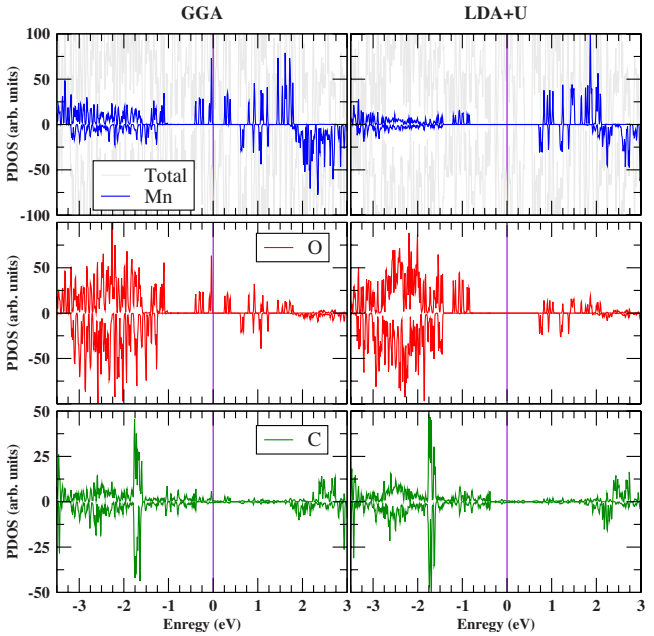

FIG. 5. (Color online) Orbital- and spin-resolved density of states around the Fermi level (vertical line at 0) for Mn_{12} attached to Au electrodes. The grey (light grey) shaded areas in the top panel represent the total DOS for the system while the blue (dark grey) areas show the Mn projected DOS. Note that the attached organic functional groups do not introduce any extra states in the vicinity of the HOMO or LUMO mainfolds (bottom two panels). In GGA, a small charge dipole between the molecule and metal surface results in a weak pinning of the HOMO state at the Fermi level.

In GGA, the HOMO level is seen to be weakly pinned at E_F, whereas in LDA+U E_F sits roughly in the middle of the HOMO-LUMO gap. This difference can be understood as follows. The vertical ionization potential of the molecule in vacuum can be estimated from a ΔSCF calculation[35] as $E_{IP}=E(N)-E(N-1)$, which is the energy difference between the neutral (N is the total number of electrons at neutrality) and singly positively charged molecule. The obtained value for E_{IP} is -6.4 eV in GGA and -6.6 eV in LDA+U. The HOMO eigenvalue ϵ_{HOMO} in LDA+U at -6.30 eV is in good agreement with $-E_{IP}$ but in GGA, ϵ_{HOMO} sits too high at -5.02 eV. This is even higher in energy than the work function of Au(111), which in this case is calculated to $-E_{IP}$ is ~5.3 eV. The level line up in the scattering region is determined roughly by how the ionization potential of the molecule in vacuum lines up relative to the work function of Au(111). Since ϵ_{HOMO} in GGA lies above E_F, when the molecule is attached to Au electrods, a small charge dipole is created. This acts to align the HOMO with the Au work function. No such dipole is created in LDA+U as ϵ_{HOMO} is already below E_F and the first empty state is well above E_F. This LDA+U picture is in good agreement with recent photoemission studies on Mn_{12} molecules deposited on Au surfaces wherein Mn $3d$ states are reported to lie roughly 1 eV below the Fermi level.[6] We note that Barraza-Lopez *et al.*[16,36] reported GGA calculations with a different level line up, where the Fermi level of Au pins the LUMO state of the Mn_{12} molecule. We attribute this difference to the small

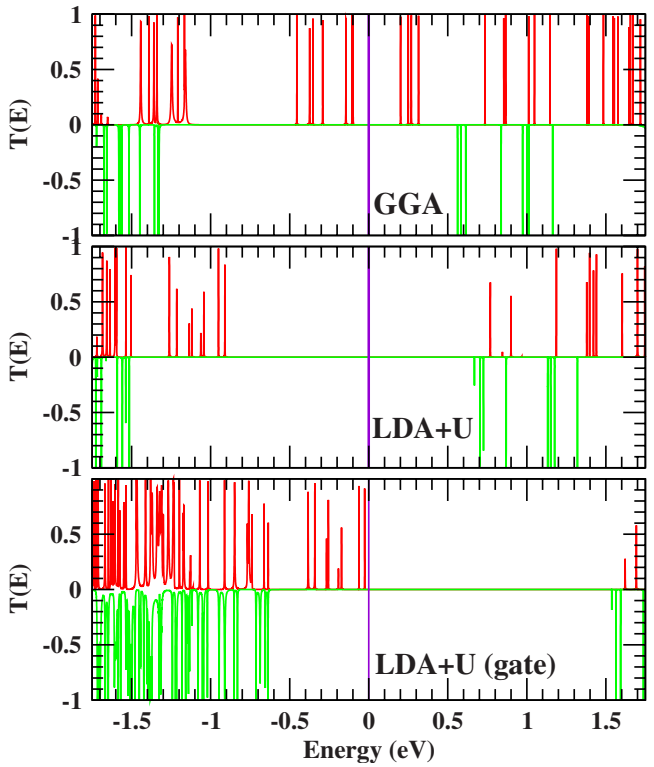

FIG. 6. (Color online) Zero-bias transmission coefficient corresponding to the scattering region shown in Fig. 4 calculated within GGA (top) and LDA+U (middle). Positive values represent the majority-spin transmission, negative values the minority-spin transmission. Note the close correspondence between the transmission peaks and the Mn-O-derived HOMO and LUMO levels (Figs. 1 and 5). The bottom panel shows the transmission coefficient in LDA +U when an additional gate voltage of 0.9 eV is applied.

HOMO-LUMO gap in GGA and possibly the use of shorter organic functional groups in their case.

In Fig. 6 we present the zero-bias transmission coefficient $T(E)$ for the system calculated both within GGA and LDA +U. The transmission peaks are seen to correspond to the Mn-O derived HOMO and LUMO states of the molecule. Furthermore, the peaks are very sharp, with a full width at half maximum of roughly 10^{-5} eV, suggesting weak coupling of the states on the Mn-O core to the electrodes. The main differences in $T(E)$ between GGA and LDA+U essentially emerge from the differences in level alignment and the nature of LUMO states discussed previously. By applying a gating potential of ~0.9 eV to the molecule in the LDA +U picture, one can align the topmost transmission peak with E_F, resulting in a very similar looking $T(E)$ to the GGA case at energies around E_F (see inset in Fig. 6). Therefore one expects the low-bias I-V properties in GGA around the HOMO manifold to be qualitatively similar to a gated LDA+U case. A similar argument also applies to the SF configuration, where the overall level alignment is essentially identical to the GS configuration except for a minority-spin transmission peak in the first set of HOMO states. In what follows, we present the finite-bias transport properties for the GS and SF configurations calculated with GGA for bias voltages of up to 400 meV. The LUMO states, whose

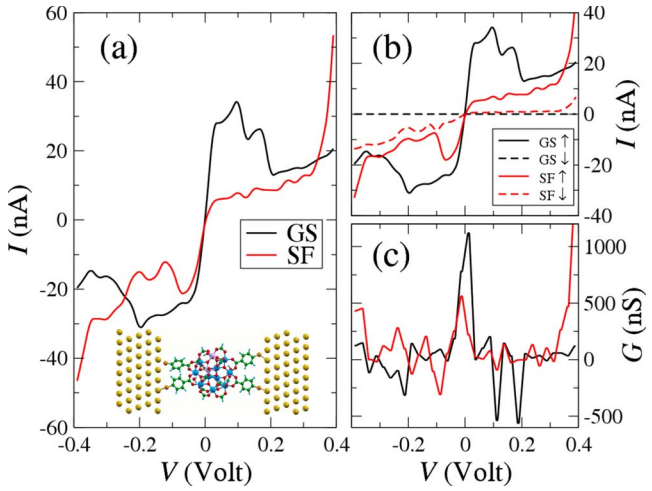

FIG. 7. (Color online) Transport properties of a Mn_{12} two-probe device. The I-V curves for both the GS and the SF configuration are presented in (a), while (b) and (c) show the I-V spin decomposition and the differential conductance, respectively. The inset in panel (a) illustrates the simulation cell.

energies are underestimated in GGA, do not contribute to the conductance for voltages under 300 meV. We then expect the LDA+U-calculated I-V curves to resemble closely the GGA ones, once the gate is applied.

V. I-V CURVES AND DISCUSSION

The calculated I-V curves, their spin decomposition, and the associated differential conductances, $G(V)$, are presented in Fig. 7 for Mn_{12} both in the GS and the SF configuration. The most notable feature is the rather stark difference between the GS and SF curves, which demonstrates that a single current readout, in principle, enables one to distinguish between the different spin states. Importantly this does not require the readout of the two spin components of the current, i.e. a spin-polarized measurement but it is simply obtained by comparing the general shape of the I-V characteristics.

In particular, the distinctive fingerprint of the two magnetic configurations is in the presence of NDRs at different bias positions for the two configurations. These originate from the dynamics of the molecular energy levels under bias,[37] their charging, and their electrical polarization. The main concept is that the different spin states of the molecule are associated to single-particle levels with different orbital symmetry and hence with different response to an external electrical potential. Thus a particular spin configuration translates into a distinct orbital configuration, which in turn is electrically readable. The details of how the various molecular orbitals respond to the external potential are then determined by their coupling to the electrodes and their charging energy.

These are investigated in Fig. 8, where we present the transmission coefficient as a function of energy, $T(E)$, calculated at different voltages for both the GS and the SF configuration. In order to understand our results let us recall the

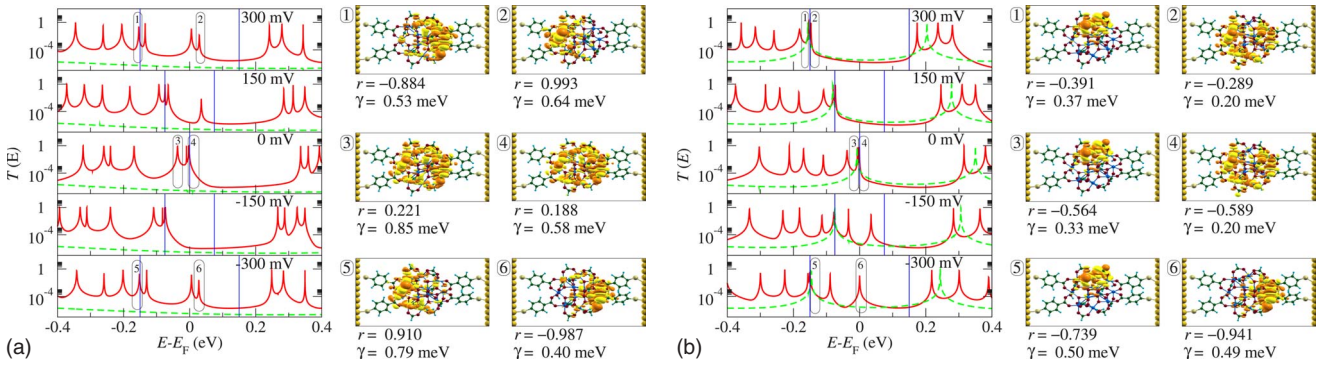

FIG. 8. (Color online) Spin-resolved transmission coefficient, $T(E)$ as a function of bias for both the GS (left) and the SF configuration (right). Red, solid (green, dashed) curves show the transmission of the majority (minority) spins. The isosurfaces display the wave functions of a number of molecular levels at different V. For these we also report the value of both r_α and γ_α. Note the dramatic rehybridization with bias leading to highly asymmetric wave functions.

main features of electron transport through a generic molecular orbital ψ_α.

When ψ_α is weakly coupled to the electrodes the associated DOS, $D_\alpha(E)$, is approximated[38] by

$$D_\alpha(E) = \frac{1}{2\pi}\frac{\gamma_\alpha}{(E-\varepsilon_\alpha)^2 + (\gamma_\alpha/2)^2}, \tag{1}$$

where $\gamma_\alpha = \gamma_\alpha^L + \gamma_\alpha^R$ and $\gamma_\alpha^L/\hbar$ ($\gamma_\alpha^R/\hbar$) are the transmission rate for electron hopping from the left-(right-) hand side electrode to ψ_α. These hopping rates γ_α^L and γ_α^R are calculated from first principles by using the spectral representation of the GF associated to the scattering region

$$G = \sum_\alpha \frac{1}{E - (\varepsilon_\alpha - i\gamma_\alpha/2) + i0^+}\psi_\alpha\tilde{\psi}_\alpha^\dagger, \tag{2}$$

where ψ_α and $\tilde{\psi}_\alpha$ are the right and left eigenvectors of H_{eff} and $(\varepsilon_\alpha - i\gamma_\alpha/2)$ are the associated eigenvalues. H_{eff} is given by

$$H_{\text{eff}} = H_M + \Sigma_L + \Sigma_R, \tag{3}$$

with H_M being the Hamiltonian of the scattering region (molecules plus part of the leads) and Σ_R (Σ_L) the self-energy for the right-(left-) hand side electrode.[14] The coupling constants γ_α^n (n=L,R) are then obtained as

$$\gamma_\alpha^n = \tilde{\psi}_\alpha^\dagger[i(\Sigma_n - \Sigma_n^\dagger)]\tilde{\psi}_\alpha. \tag{4}$$

One can easily demonstrate that with this definition $\gamma_\alpha = \gamma_\alpha^L + \gamma_\alpha^R$.

The single-particle energy ε_α depends on the charging state of the molecule. In mean-field approximation ε_α scales linearly[17] with the orbital occupation, n_α, which in turn is determined by

$$n_\alpha = \int_{-\infty}^{+\infty} dE D_\alpha(E)\frac{\gamma_\alpha^L f^L(E) + \gamma_\alpha^R f^R(E)}{\gamma_\alpha}. \tag{5}$$

Here f^L (f^R) is the Fermi function evaluated at $E-\mu_L$ ($E-\mu_R$) with μ_L (μ_R) the chemical potential of the left-(right-) hand side electrode ($\mu_L - \mu_R$=eV). Finally the transmission coefficient is

$$T_\alpha(E) = 2\pi\gamma_\alpha^L\gamma_\alpha^R D_\alpha(E)/\gamma_\alpha. \tag{6}$$

The expression (5) establishes that the steady-state current is a balance of electron fluxes to and from both the electrodes. Thus if a molecular level is more strongly coupled to one of the electrodes, as in an STM geometry, its single-particle energy will be pinned to the chemical potential of that electrode, and the corresponding transmission peak $T(\varepsilon_\alpha)$ will move in energy as a function of bias accordingly. In contrast, when $\gamma_\alpha^L \approx \gamma_\alpha^R$, then $T_\alpha(\varepsilon_\alpha)$ as a function of V is only determined by the level charging energy. Crucially in both the situations the level broadening γ_α does not depend on bias and the width of the transmission peak does not change with V. As a consequence $I(V)$ is solely determined by the *position* of the transmission peaks. Since upon increasing the bias charging alone cannot expel from the bias window a molecular level which is already inside at a lower bias, no NDRs are expected. This is the most typical situation in molecular junctions.

In contrast the picture presented in Fig. 8 is rather different. Let us take the GS as an example. At V=0 the first four HOMOs are less then 50 meV from E_F and approximately 300 meV away from the first of the LUMO, hence they determine the low-bias current. At positive bias the current is initially determined by the first HOMO, which is pinned at E_F. The HOMO moves into the bias window at about 100 mV and then roughly maintains its energy position at any larger positive V. Notably for $V<100$ mV the height of $T(\varepsilon_{\text{HOMO}})$ is near to 1, suggesting that such a state is equally coupled to the electrodes. However when the level completely enters the bias window $T(\varepsilon_{\text{HOMO}})$ reduces dramatically (note that the scale of Fig. 8 is logarithmic), indicating that now the coupling to the electrodes has changed. In general the magnitude of $T(\varepsilon_\alpha)$ reduces if $\gamma_\alpha^L \neq \gamma_\alpha^R$. We then conclude that for the HOMO the coupling to the electrodes becomes asymmetric with bias.

As mentioned before we extract quantitative parameters describing the dynamic coupling between the electrodes and the molecular orbitals as a function of bias from the spectral representation of the nonequilibrium Green's function. For each molecular level ψ_α, one can evaluate the contributions to the imaginary part of the self-energy originating, respec-

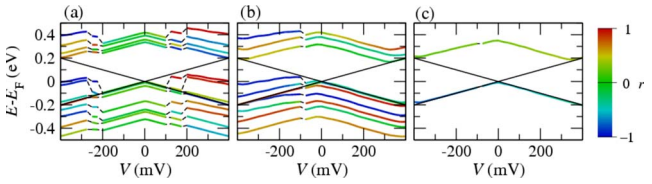

FIG. 9. (Color online) Trace of r_α as a function of energy and bias. The colored lines denote the position of the peaks in the transmission coefficient and the color encodes the magnitude of r_α. The two solid straight black lines mark the boundaries of the bias window. Panel (a) is for the GS and majority spins, panel (b) is for the SF configuration and majority spins, and panel (c) is for the SF configuration and minority spins. Color code: red $r_\alpha=1$, green $r_\alpha=0$, blue $r_\alpha=-1$.

tively, from the electronic coupling to the left ($\gamma_\alpha^{\mathrm{L}}$) and right ($\gamma_\alpha^{\mathrm{L}}$) electrode. In addition to the total broadening γ_α we now can define the coupling asymmetry parameter $r_\alpha=(\gamma_\alpha^{\mathrm{L}}-\gamma_\alpha^{\mathrm{R}})/(\gamma_\alpha^{\mathrm{L}}+\gamma_\alpha^{\mathrm{R}})$. This is +1 (−1) for molecular orbitals more strongly coupled to the left (right) contact and 0 for coupling equally strong to both the electrodes.

In the Figs. 9 and 10 we trace ε_α from the position of the various peaks in the transmission coefficients as a function of V. The colors encode the value of r_α (in Fig. 9) and γ_α (in Fig. 10), and the two straight black lines mark the bias window. Let us start again from the GS [panels (a)]. As mentioned before for small V the first HOMO is pinned to the lower bound of the bias window and, confirming our initial guess, it is roughly equally coupled to the electrodes [Fig. 9(a)]. However for $V\sim 100$ mV it suddenly jumps into the bias window. In doing so a remarkable effect takes place: its coupling to the leads becomes extremely asymmetric, $r_\alpha \sim 1$ while γ_α remains approximately constant. Considering the fact that the contribution to the current from a transmission peak, I_α, is approximately

$$I_\alpha = 2\pi\frac{e}{h}\frac{\gamma_\alpha(1-r_\alpha^2)}{4}, \tag{7}$$

we conclude that as soon as the peak enters the bias window the total current actually decreases. This creates the NDR at 100 mV shown in Fig. 7(c). Similarly the second HOMO enters the bias window at 200 mV, again with a drastic change in r_α. This produces the second NDR at 200 mV.

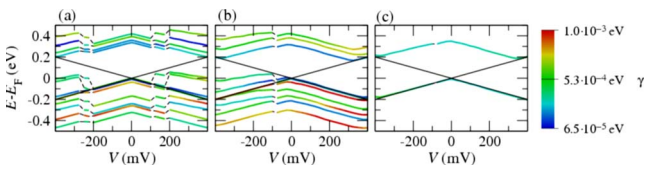

FIG. 10. (Color online) Trace of γ_α as a function of energy and bias. The colored lines denote the position of the peaks in the transmission coefficient and the color encodes the magnitude of γ_α. The two solid straight black lines mark the boundaries of the bias window. Panel (a) is for the GS and majority spins, panel (b) is for the SF configuration and majority spins, and panel (c) is for the SF configuration and minority spins. Color code: red $\gamma_\alpha=10^{-3}$ eV, blue $\gamma_\alpha=6.5\times10^{-5}$ eV.

For $V<0$ the situation is analogous although quantitatively different. Again at low bias the HOMO follows the lower boundary of the bias window with an almost equal coupling to the two electrodes. Then at about −200 mV it suddenly enters the bias window together with the HOMO-2. Similarly to the $V>0$ case entering into the bias window is accompanied by a drastic change in coupling. This time however $r_\alpha\sim-1$, indicating that the molecular level is now more strongly coupled to the right-hand side electrode. As a result the NDRs at negative V appears only at −200 mV.

We now turn our attention to the SF configuration. The most notable feature is represented by the minority HOMO, for which the coupling to the leads is almost insensitive to the bias and it is rather equally strong to both the electrodes [see Figs. 9(c) and 10(c)]. Therefore the level always follows the lower boundary of the bias window and remains occupied at any voltage, thus resulting in an almost linear contribution to the I-V. The majority component of the current instead displays a behavior qualitatively similar to that of the GS. This time however the first two HOMOs enter the bias window together but only at negative voltages (around −100 mV), again in correspondence to an increased asymmetry of the electronic coupling with the electrodes [$r_\alpha\sim-1$, see Fig. 9(b)]. This generates the NDR at −100 mV.

Finally we answer the following question: what is the mechanism behind the bias dependence of r_α? Let us consider the isosurfaces of Fig. 8, displaying the electronic wave function of a given molecular level in presence of V. For example, let us look at the panels 2, 4, and 6 for the GS. These represent the wave function of the first HOMO, respectively, at 300, 0, and −300 mV. Clearly as bias is applied, the wave function experiences a substantial polarization, with the electron clouds changing from a uniform distribution at $V=0$ to one which is considerably localized either to the left- or to the right-hand side of the junction. The molecular-orbital distortion under bias originates from molecular-orbital rehybridization and always involves a number of molecular states. For instance, when the HOMO and HOMO-1 enter the bias window at $V>0$ the rehybridization involves the first several HOMOs, as one can deduce from the fact that for most of them there is a change in r_α [see Fig. 9(a)]. Importantly for the SF configuration there is only one minority-spin level around E_{F}, this cannot hybridize with any other state (unless a spin-flip event occurs), and therefore its coupling to the electrodes changes little with bias. This fundamental aspect is what creates profoundly different I-V curves in the two cases.

Crucially orbital rehybridization results in the molecular levels entering the bias window always to display largely asymmetric coupling to the electrodes. This allows them to enter the bias window and to conduct without charging the molecule, which remains neutral at any bias investigated. We therefore conclude that the observed NDRs are features in the I-V occurring at energies lower than the typical charging energy of the molecule. Note that in general orbital rehybridization may not only lead to NDRs but also to a sharp increase in $G(V)$. Importantly these are always low-energy satellite features to the main Coulomb blockade signal.

VI. CONCLUSION

In conclusion, we have calculated the bias-dependent transport properties of Mn_{12} SMMs attached to nonmagnetic Au electrodes within a first-principles framework. The electronic-structure and zero-bias transport properties of the system were calculated both using standard GGA and also by incorporating on-site Hubbard-U corrections at the LDA $+U$ level. We find the ionization potential and the HOMO-LUMO gap of Mn_{12} to be underestimated in GGA but an appropriate choice of the U parameter within LDA$+U$ leads to good agreement with experimental photoemission data. Significantly, the orbital character of the HOMO manifold of states is found to be the same both within GGA and LDA $+U$. Therefore, the low-bias transport properties within GGA are expected to be qualitatively similar to that of a device where the molecule is gated. Electron transport through the system is primarily of tunneling character with the Mn-O core of the Mn_{12} SMM being weakly coupled to the electrodes via the organic functional groups. In the out-of-equilibrium situation, a bias-driven rehybridization of the molecular orbitals is observed which leads to a drastic change in the way the levels are coupled to the electrodes, going from approximately symmetric coupling near zero bias to highly asymmetric coupling at larger bias. This in turn leads to sudden changes in the conductance with bias which in this case manifest as regions of NDR in the I-V. In general, we expect such a rehybridization mechanism to occur in any system that presents a number of closely spaced molecular levels close to the electrodes' Fermi level. However, single molecules magnets, with their d-electron manifold, appear as the ideal material system for such an effect. Interestingly, this mechanism is also seen to be sensitive to the internal spin configuration of the molecule because of the differences in the charge distributions corresponding to different spin configurations. In particular, features in the I-V such as the NDRs occur at different bias voltages for the two different spin configurations studied. This suggests that in systems such as SMMs, an electrical readout might be able to distinguish between two different magnetic configurations, without the need for resolving the two spin components of the current.

ACKNOWLEDGMENTS

We thank Greg Szluncheski for interesting discussions and Roberta Sessoli for having driven our attention towards Mn_{12} and for having provided us with crystallographic data on Mn_{12}. This work is sponsored by Science Foundation of Ireland (Grants No. 07/IN.1/I945 and No. 07/RFP/PHYF235) and by the European Union (Grant No. SpiDME EC-FP6 NEST). Computational resources have been provided by the HEA IITAC project managed by the Trinity Centre for High Performance Computing and by the Irish Center for High-End Computing.

[1] D. Gatteschi, R. Sessoli, and J. Villain, *Molecular Nanomagnets* (Oxford University Press, Oxford, 2006).
[2] H. B. Heersche, Z. de Groot, J. A. Folk, H. S. J. van der Zant, C. Romeike, M. R. Wegewijs, L. Zobbi, D. Barreca, E. Tondello, and A. Cornia, Phys. Rev. Lett. **96**, 206801 (2006).
[3] M.-H. Jo, Jacob E. Grose, Kanhayalal Baheti, Mandar M. Deshmukh, Jennifer J. Sokol, Evan M. Rumberger, David N. Hendrickson, Jeffrey R. Long, Hongkun Park, and D. C. Ralph, Nano Lett. **6**, 2014 (2006).
[4] C. Romeike, M. R. Wegewijs, and H. Schoeller, Phys. Rev. Lett. **96**, 196805 (2006).
[5] C. Romeike, M. R. Wegewijs, M. Ruben, W. Wenzel, and H. Schoeller, Phys. Rev. B **75**, 064404 (2007).
[6] S. Voss, M. Fonin, U. Rüdiger, M. Burgert, U. Groth, and Yu. S. Dedkov, Phys. Rev. B **75**, 045102 (2007).
[7] M. Mannini, P. Sainctavit, R. Sessoli, C. Cartier dit Moulin, F. Pineider, M.-A. Arrio, A. Cornia, and D. Gatteschi, Chem.-Eur. J. **14**, 7530 (2008).
[8] M. Mannini, F. Pineider, P. Sainctavit, L. Joly, A. Fraile-Rodrguez, M.-A. Arrio, C. Cartier dit Moulin, W. Wernsdorfer, A. Cornia, D. Gatteschi and R. Sessoli, Adv. Mater. (Weinheim, Ger.) **21**, 167 (2009).
[9] S. Voss, M. Fonin, U. Rüdiger, M. Burgert, and U. Groth, Appl. Phys. Lett. **90**, 133104 (2007).
[10] G.-H. Kim and T.-S. Kim, Phys. Rev. Lett. **92**, 137203 (2004).
[11] Maciej Misiorny and Józef Barnaś, Phys. Rev. B **76**, 054448 (2007).
[12] Florian Elste and Carsten Timm, Phys. Rev. B **75**, 195341 (2007).
[13] Gabriel González, Michael N. Leuenberger, and Eduardo R. Mucciolo, Phys. Rev. B **78**, 054445 (2008).
[14] A. R. Rocha, V. M. Garcia-Suarez, S. Bailey, C. Lambert, J. Ferrer, and S. Sanvito, Phys. Rev. B **73**, 085414 (2006).
[15] A. R. Rocha, V. M. Garcia Suarez, S. W. Bailey, C. J. Lambert, J. Ferrer, and S. Sanvito, Nature Mater. **4**, 335 (2005).
[16] Salvador Barraza-Lopez, Kyungwha Park, Víctor García-Suárez, and Jaime Ferrer, J. Appl. Phys **105**, 07E309 (2009).
[17] C. Toher, A. Filippetti, S. Sanvito, and K. Burke, Phys. Rev. Lett. **95**, 146402 (2005).
[18] C. Toher and S. Sanvito, Phys. Rev. Lett. **99**, 056801 (2007).
[19] C. Toher and S. Sanvito, Phys. Rev. B **77**, 155402 (2008).
[20] Note that this is simply a broken symmetry configuration and that such a state is not an eigenstate of the total spin operator. More on this aspect can be found in: L. Noodleman, J. Chem. Phys. **74**, 5737 (1981).
[21] J. M. Soler, E. Artacho, J. D. Gale, A. Garcia, J. Junquera, P. Ordejón, and D. Sanchez-Portal, J. Phys.: Condens. Matter **14**, 2745 (2002).
[22] J. P. Perdew, K. Burke, and M. Ernzerhof, Phys. Rev. Lett. **77**, 3865 (1996).
[23] S. L. Dudarev, G. A. Botton, S. Y. Savrasov, C. J. Humphreys, and A. P. Sutton, Phys. Rev. B **57**, 1505 (1998).
[24] M. Wierzbowska, D. Sánchez-Portal, and S. Sanvito, Phys. Rev. B **70**, 235209 (2004).
[25] S. Datta, *Electronic Transport in Mesoscopic Systems* (Cambridge University Press, Cambridge, UK, 1995).

[26] C. Caroli, R. Combescot, P. Nozieres, and D. Saint-Janes, J. Phys. C **5**, 21 (1972).
[27] I. Rungger and S. Sanvito, Phys. Rev. B **78**, 035407 (2008).
[28] Z. Zeng, D. Guenzburger, and D. E. Ellis, Phys. Rev. B **59**, 6927 (1999).
[29] M. R. Pederson and S. N. Khanna, Chem. Phys. Lett. **307**, 253 (1999); Phys. Rev. B **59**, R693 (1999).
[30] M. R. Pederson and S. N. Khanna, Phys. Rev. B **60**, 9566 (1999).
[31] D. W. Boukhvalov, A. I. Lichtenstein, V. V. Dobrovitski, M. I. Katsnelson, B. N. Harmon, V. V. Mazurenko, and V. I. Anisimov, Phys. Rev. B **65**, 184435 (2002).
[32] C. Franchini, V. Bayer, R. Podloucky, J. Paier, and G. Kresse, Phys. Rev. B **72**, 045132 (2005).
[33] D. W. Boukhvalov, M. Al-Saqer, E. Z. Kurmaev, A. Moewes, V. R. Galakhov, L. D. Finkelstein, S. Chiuzbäian, M. Neumann, V. V. Dobrovitski, M. I. Katsnelson, A. I. Lichtenstein, B. N. Harmon, K. Endo, J. M. North, and N. S. Dalal, Phys. Rev. B **75**, 014419 (2007).
[34] I. Mirebeau, M. Hennion, H. Casalta, H. Andres, H. U. Güdel, A. V. Irodova, and A. Caneschi, Phys. Rev. Lett. **83**, 628 (1999).
[35] L. Hedin and A. Johansson, J. Phys. B **2**, 1336 (1969).
[36] Salvador Barraza-Lopez, Michael C. Avery, and Kyungwha Park, Phys. Rev. B **76**, 224413 (2007).
[37] A. R. Rocha and S. Sanvito, Phys. Rev. B **70**, 094406 (2004).
[38] S. Datta, Nanotechnology **15**, S433 (2004).